# Soft Matter

## Accepted Manuscript

This article can be cited before page numbers have been issued, to do this please use: K. Shibata, H. Kanda, Y. Tanaka and Y. Sumino, *Soft Matter*, 2026, DOI: 10.1039/D6SM00232C.




ROYAL SOCIETY OF CHEMISTRY

rsc.li/soft-matter-journal

View Article Online
DOI: 10.1039/D6SM00232C

Soft Matter

ARTICLE TYPE

Cite this: DOI: 00.0000/xxxxxxxxxx

# Elastocapillary lifting and encapsulation of water by a triangular elastic film under gravity

Kyoko Shibata,[a†] Hana Kanda,[b†], Yoshimi Tanaka[b] and Yutaka Sumino[a,c,d,*]

Received Date
Accepted Date

DOI: 00.0000/xxxxxxxxxx

We investigate the encapsulation of water by a thin elastic film as a minimal model of elastocapillary self-folding with fluid transport. An equilateral triangular polydimethylsiloxane film is lifted quasi-statically from a water surface, while its side length and thickness are systematically varied. Depending on these parameters, the film exhibits three distinct morphologies: folding, recoiling, and liquid encapsulation. We show that the morphology is governed by the interplay of surface, gravitational, and bending energies, and that encapsulation occurs only within a narrow parameter region where the elastocapillary, elastogravity, and capillary length scales become comparable. This provides a simple physical criterion for liquid encapsulation by elastic films.

## 1 Introduction

Interfacial tension dominates gravitational effects when the characteristic length of a system becomes smaller than the capillary length, $L_{cg} = \sqrt{\gamma/(\rho g)}$. Under such conditions, capillary forces can drive counterintuitive fluid motions, such as capillary rise and the spontaneous climbing of droplets against gravity[1–4]. These phenomena originate from the tendency of interfacial tension to minimize surface area, leading to cohesive interactions between fluids and surrounding structures. When the characteristic length scale is sufficiently small, this balance between surface energy and gravity provides a simple physical framework for understanding a wide range of capillarity-driven behaviors.

When solid boundaries interacting with a liquid are soft and deformable, interfacial tension can induce significant elastic deformation, leading to elastocapillary phenomena. A droplet on an elastomer creates ridges at its contact line, thereby modifying its wetting dynamics[5]. Similarly, thin elastic filaments can undergo spontaneous twisting driven by the draining of liquids[6], and micro to nanoscale resist structures may collapse during drying due to capillary forces[7]. These examples demonstrate that elastocapillary effects not only alter local wetting behavior but can trigger large-scale deformations of soft solids. Such deformation of soft boundaries, in turn, can strongly influence the dynamics of interacting fluids. Beyond engineered systems, similar elastocapillary and capillarity-driven mechanisms are widely exploited in nature, for example, in the water-collecting structures of plants[8–10], the locomotion of water-walking insects[11–13], and emerging soft robotic systems[14,15].

Exploiting the coupling between elasticity and capillarity, capillary origami enables the spontaneous formation of three-dimensional structures from two-dimensional elastic films[16,17]. By appropriately designing the film shape, such self-folding can be harnessed to capture and lift liquid droplets[18]. In their study, the folding behavior and resulting functions were primarily controlled by modifying the film geometry, for example, through the number of petals. Related approaches have also demonstrated elastomer-based devices capable of liquid pipetting driven by capillary forces[19].

Despite these advances, the physical criteria governing the onset of liquid encapsulation and self-folding remain unclear, particularly in relation to the competing roles of elasticity, surface tension, and gravity. In this study, we address this issue by systematically varying the side length and thickness of an equilateral triangular film. This minimal geometry allows us to construct a phase diagram for elastocapillary self-folding and liquid encapsulation, which we interpret using characteristic length scales associated with bending, capillarity, and gravity.

In the work by Reis et al.[18], the film geometry was optimized into a petal-like shape to achieve controlled deformation. Nakamura et al.[19] employed fixed flower-like geometries and treated the lifting speed and gravity direction as control parameters. In the present study, by contrast, we focused on a minimal equilateral triangular film and observed three deformation morphologies corresponding to folding, recoiling, and liquid encapsulation. Whereas previous studies achieved encapsulation using specifically designed geometries such as petal-shaped films[18], the

[a]Department of Applied Physics, Tokyo University of Science, 6-3-1 Nijuku, Katsushika-ku, Tokyo 125-8585, Japan.
[b]Graduate School of Innovative and Practical Studies, Yokohama National University, Yokohama 240-8501, Japan.
[c]WaTUS and DCIS, Research Institute for Science & Technology, Tokyo University of Science, 6-3-1 Nijuku, Katsushika-ku, Tokyo 125-8585, Japan.
[d]Faculty of Engineering and Physical Sciences, University of Surrey, Guildford, Surrey GU2 7XH, United Kingdom.
*E-mail: ysumino@rs.tus.ac.jp
† These authors contributed equally to this work.

View Article Online
DOI: 10.1039/D6SM00232C



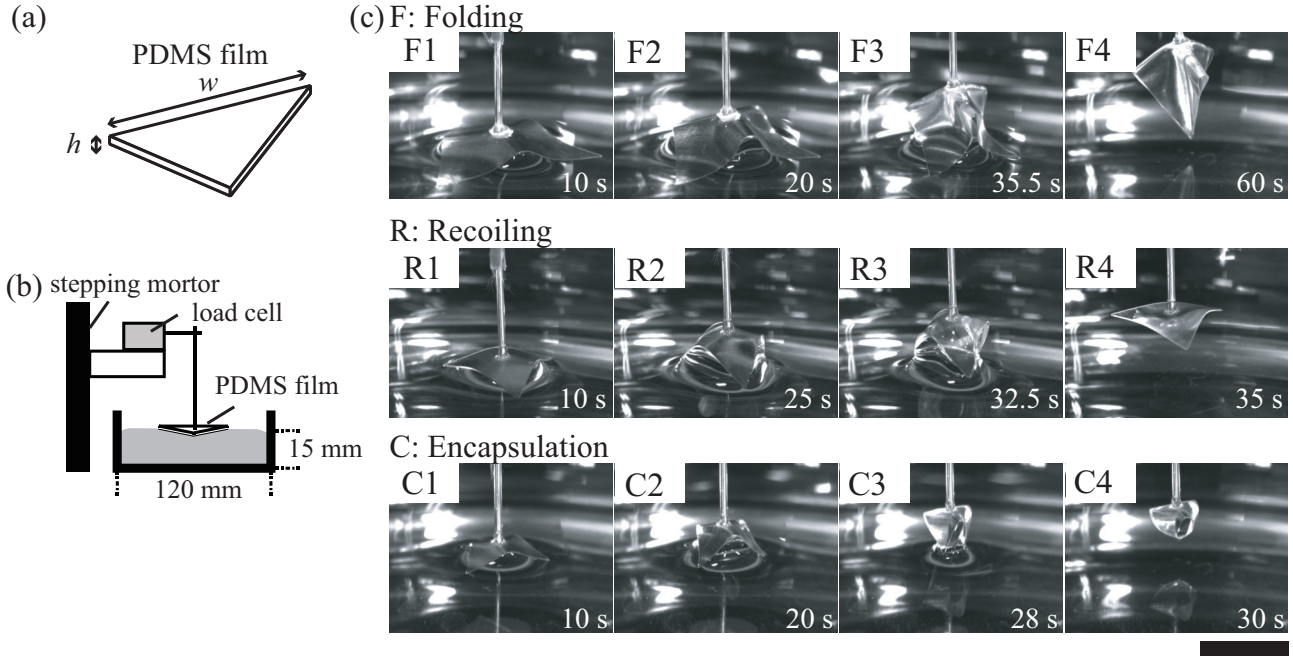


Fig. 1 (a) Geometry of the PDMS film. The film thickness $h$ and side length $w$ were systematically varied. (b) Schematics of experimental setup. The PDMS film was lifted vertically from the water surface by a wire attached at its center. (c) Representative snapshots showing three deformation morphologies of the film: folding (F; $h = 98$ μm, $w = 20$ mm), recoiling (R; $h = 132.25$ μm, $w = 12.5$ mm), and encapsulation (C; $h = 98$ μm, $w = 10$ mm). The time $t = 0$ corresponds to the onset of lifting. Scale bar: 10 mm.

present study demonstrates that encapsulation can emerge even in a simple triangular geometry through the competition between elastocapillary, elastogravity, and capillary length scales. This provides a more general physical criterion that is not tied to a particular geometric design. We further tested this interpretation by varying the surface tension of the aqueous phase using surfactant solutions.

In the following sections, we describe an experimental system in which an equilateral triangular elastic film is lifted quasi-statically from a water surface while its side length and thickness are systematically varied. Depending on these parameters, the film undergoes folding, recoiling, or liquid encapsulation. We analyze these behaviors in terms of the competition between bending, capillary, and gravitational effects.

## 2 Experimental setup

### 2.1 Sample preparation

Elastic films with thickness $h = 38$–$160\ \mu$m made of polydimethylsiloxane (PDMS) were prepared following standard procedures. The base and curing agents of SILPOT 184 (Dow Chemical) were mixed at a weight ratio of 10:1. The mixture was spin-coated onto a PTFE substrate at rotation speeds ranging from 500 to 1500 rpm to form thin films. The films were then cured at 100 °C for 1 h to obtain elastic PDMS sheets. After curing, the films were cut into equilateral triangular shapes with a side length $w$, as shown in Fig. 1(a). The Young's modulus of the PDMS film was taken as $E = 0.7 \times 10^6$ Pa[20].

The liquids used in this study were pure water and a 30 mM aqueous solution of Polyethylene Glycol Mono-4-octylphenyl Ether (Triton X). Pure water was prepared using a Millipore Milli-Q system. Triton X was purchased from Tokyo Chemical Industry Co., Ltd. (P0873). The density $\rho$ of both liquids was assumed to be $1.0 \times 10^3\,\mathrm{kg\,m^{-3}}$. The surface tension of water, $\gamma_w$, was taken as $72\,\mathrm{mN\,m^{-1}}$, whereas that of the Triton X solution, $\gamma_T$, was taken as $30\ \mathrm{mN\,m^{-1}}$, since the Triton X concentration (30 mM) is well above the critical micelle concentration (CMC ≈ 0.2–0.3 mM). Here, $\gamma_i$ denotes the surface tension of the liquid phase, where $i = w$ or $T$.

### 2.2 Experimental apparatus

The schematic experimental setup is shown in Fig. 1(b). Pure water was placed in a Petri dish with a diameter of 120 mm and a depth of 15 mm. The elastic film was attached at its center to an iron wire using cyanoacrylate adhesive (Aron Alpha, Toagousei Co., Ltd.). The wire was connected to a load cell (LVS-5VGA, Kyowa Electronic Instruments Co., Ltd.) mounted on a vertical translation stage driven by a stepping motor (SGSP20-35, Sigma Koki Co., Ltd.).

The film was initially positioned at the water surface and then lifted vertically at a constant speed of $1\ \mathrm{mm\,s^{-1}}$. The deformation of the film during lifting was recorded using a CMOS camera (DMK37BUX273, The Imaging Source) at 20 Hz. The force measured by the load cell was recorded using a data logger (GL7000, Graphtec Co.) and used to evaluate the weight of the lifted water, denoted by $mg$. The value before lifting the film from the water surface was defined as zero, and the increase from this value was plotted as the apparent lifted weight in Fig. 2(b,d). Although the measured force includes the contribution from the film itself, the film weight is at most 0.1 mN (for $w = 20$ mm and $h = 150\ \mu$m), which is negligible compared with the measured force. Therefore,

View Article Online
DOI: 10.1039/D6SM00232C



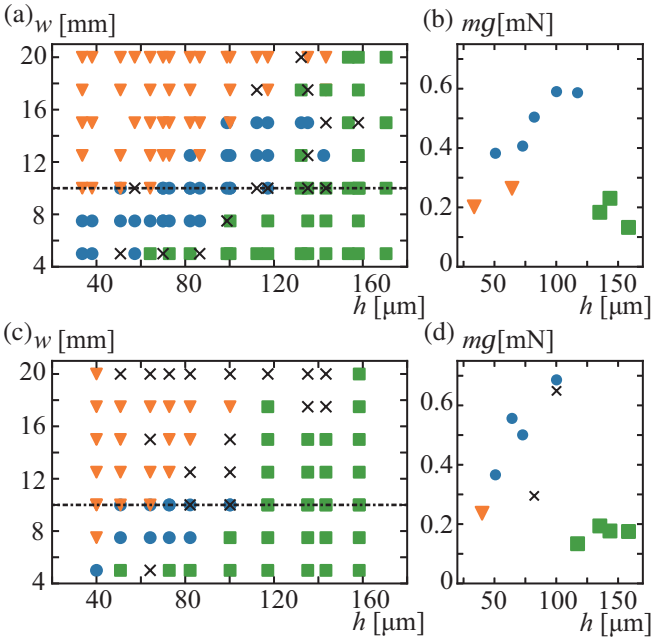


Fig. 2 (a,c) Phase diagrams of the deformation morphologies of the lifted film as functions of film thickness $h$ and side length $w$ for (a) pure water and (c) Triton X solution. Orange triangles, green squares, and blue circles correspond to the folding, recoiling, and encapsulation regimes, respectively [see Fig.1(c)]. The morphologies were classified based on the final film configuration observed during lifting. The dashed line indicates the parameter set used in panels (b,d). All experimental data points are shown in the phase diagrams. (b,d) Apparent weight of the liquid lifted by the film, $mg$, as a function of film thickness $h$ for a fixed side length of $w$=10mm, measured for (b) pure water and (d) Triton X solution.

the measured force mainly reflects the weight of the water lifted by the film.

## 3 Results

When an elastic film was lifted from the surface of a liquid, distinct deformation morphologies were observed depending on the film thickness and side length. As shown in Fig. 1(c), the film exhibited folding, recoiling, and liquid encapsulation. In the following, we first describe these representative morphologies and then summarize them in a phase diagram.

### 3.1 Deformation morphologies of elastic films

As shown in Fig. 1(c), the film initially lifted liquid due to wetting of the PDMS film surface in all cases. When the film was sufficiently thin, it folded spontaneously with threefold symmetry around the attached wire while the liquid was gradually drained away [Fig. 1(c:F1-4)]. In contrast, when the film was sufficiently rigid to resist deformation, it recoiled back to a nearly flat shape, while retaining only a small droplet at its bottom [Fig. 1(c:R1-4)]. In an intermediate parameter range between these two regimes, liquid encapsulation was observed, in which the liquid was spontaneously wrapped inside the film [Fig. 1(c:C1-4)].

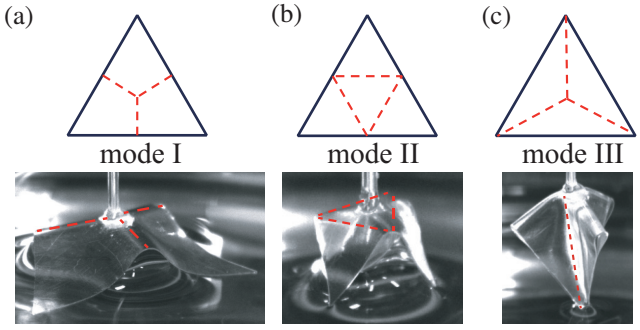


Fig. 3 Characteristic deformation modes of the elastic film, classified as (a) Mode I, (b) Mode II, and (c) Mode III. The dashed lines indicate regions of large mean curvature. Bottom images show the corresponding regions of high mean curvature in the experimental snapshots shown in Fig. 1(c).

### 3.2 Phase diagram of film morphologies

Fig. 2(a) shows the phase diagram of the observed film morphologies as a function of film thickness $h$ and side length $w$. The deformation morphologies were classified based on the final film configuration. Three distinct regions corresponding to folding, recoiling, and encapsulation morphologies are identified. The encapsulation morphology appears in an intermediate region between the folding and recoiling regimes. A small number of marginal cases, where mixed or asymmetric behaviors were observed, are also indicated.

The liquid encapsulation regime is further characterized by the weight of the lifted liquid, $mg$, as shown in Fig. 2(b). These data were obtained for films with a fixed side length $w$=10 mm. Larger values of $mg$ were observed when the film exhibited the encapsulation morphology. As the system transitions from folding to encapsulation, the lifted liquid weight increases gradually. In contrast, a sharp decrease in $mg$ was observed when the system transitions from encapsulation to recoiling at larger $h$.

In addition to these dominant behaviors, marginal cases were observed, including intermediate encapsulation–recoiling states, where the deformed film retained a finite liquid droplet at its bottom, as well as asymmetric folding without threefold symmetry. These marginal events are indicated by black crosses in Fig. 2 (a) and (b).

We have also conducted additional experiments using a Triton X solution. The corresponding results are shown in Fig. 2(c) and (d). The phase diagram is shifted toward the lower-left corner, and the parameter region for the encapsulation regime becomes smaller. The lifted liquid weight shown in Fig. 2(d) also exhibits a strong dependence on the observed morphology.

We also examined the effect of lifting speed and liquid viscosity on the final morphology. The lifting speed was varied from 0.1 to 30 $\mathrm{mm\,s^{-1}}$. The liquid viscosity was varied from approximately 1 mPa s (pure water) to 50 mPa s using a 30 wt.% PEG6000 aqueous solution. However, no substantial change in the final morphology was observed. Under these conditions, the capillary number, $Ca = \mu V/\gamma_i$, ranged from approximately $10^{-6}$ in the standard experimental condition to $10^{-1}$, but remained below unity. The Reynolds number $Re = \rho LV/\mu$ remained of order unity or

View Article Online
DOI: 10.1039/D6SM00232C



smaller in the present system. The Weber number $We = \rho V^2 L/\gamma_l$ ranged from $10^{-4}$ to $10^{-1}$, indicating that inertial effects are negligible. These observations indicate that viscous effects associated with the lifting motion do not dominate the morphology selection within the accessible experimental range. We therefore focus on the quasi-static balance between bending, capillary, and gravitational effects.

## 4 Discussion

### 4.1 Deformation modes of elastic films

The deformation morphology observed in the lifting process can be interpreted in terms of three characteristic deformation modes (Mode I–III), as illustrated in Fig. 3(a-c). These modes preserve the threefold symmetry of the equilateral triangular film and are distinguished by the locations of regions of high curvature.

In the folding regime, the deformation is initially dominated by Mode I [Fig. 3(a)], where ridges form along lines connecting the lifting point to the midpoints of the film edges. Geometrical constraints at the vertices due to capillary force at the air-water interface prevent vertical deformation, leading to the coexistence of Mode I and Mode III [Fig. 3(c)] at later stages. This combined deformation ultimately results in expulsion of the liquid.

In contrast, recoiling behavior is associated with Mode II [Fig. 3(b)], in which the regions near the vertices bend downward. As the film is lifted, capillary breaking occurs, and the elastic energy stored in the film drives the system back to a nearly flat configuration.

Liquid encapsulation emerges in an intermediate regime, where the deformation evolves from a mixed Mode I–II configuration toward a Mode II–dominated state. In this case, the approach of the three vertices facilitates the formation of a transient liquid bridge, which subsequently undergoes capillary breaking to form a closed capsule.

These deformation modes are not universally traversed in all cases; rather, each observed behavior follows a distinct deformation pathway. The central attachment point enforces a symmetric boundary condition, which stabilizes the threefold deformation patterns but does not qualitatively alter the underlying energy balance. This classification allows us to interpret the phase diagram in terms of transitions between dominant deformation modes.

### 4.2 Energy competition and morphology selection

Here we discuss the simplified energy estimates. The relevant energies in the present system are bending energy $U_b$, gravitational energy $U_g$, and surface energy $U_s$. Here, $U_b \sim BA\kappa^2$, $A$ is the deformed area, and $\kappa$ is the curvature of deformation. $U_g \sim \rho g V \Delta z$, where $V$ is the volume of lifted water, and $\Delta z$ is the lifted height of water. Finally, $U_s \sim \gamma_l S$, where $S$ is the area of wetted surface.

For the recoiling state, capillary deformation is insufficient to stabilize large bending deformation, and the dominant contribution is the surface energy associated with the wetted triangular area of the film, $U_r \approx \zeta \gamma_l w^2$. For the folding state, $U_f \approx \xi B w/\ell_{\mathrm{ridge}} = \xi B w/L_{ec}$, where the bending energy is assumed to be localized along the three ridges (Fig. 3(a):Mode I) with length $w/(2\sqrt{3})$, where $\ell_{\mathrm{ridge}} \sim L_{ec}$, following the estimation of loop structures in [16,21]. For the encapsulated state, we estimate $U_c \sim \alpha \rho g w^4 + \varepsilon B$, where the first term represents the gravitational potential energy of the encapsulated liquid volume and the second term represents the bending cost of the capsule.

Table 1 Variables used for dimensional analysis

| Variable | description | values |
|---|---|---|
| $E$ | Young's modulus | $0.7 \times 10^6$ Pa |
| $\nu$ | Poisson's ratio | 0.5 |
| $\rho$ | density of water | $1.0 \times 10^3$ kg m$^{-3}$ |
| $g$ | Gravitational acceleration | 10 m s$^{-2}$ |

Using simple geometric estimates for these energies, we constructed an energy-minimum phase diagram shown in Fig. 5. Despite the simplified assumptions, the obtained phase structure reproduces the experimentally observed morphology sequence and its shift upon reducing surface tension. These results support the interpretation that liquid encapsulation emerges in the crossover regime where bending, capillary, and gravitational effects become comparable.

### 4.3 Emergence of characteristic length scales

The phase behavior observed in the present experiments can be interpreted in terms of a characteristic lateral deformation scale $L$, namely the elastogravity length $L_{eg}$ [18] and the elastocapillary length $L_{ec}$ [18]. These characteristic lengths are given by

$$L_{eg} = \left(\frac{B}{\rho g}\right)^{1/4}, \; L_{ec} = \left(\frac{B}{\gamma_l}\right)^{1/2} \tag{1}$$

These characteristic lengths provide natural criteria for comparing the effective deformation scale $L$ with the relevant elastocapillary and elastogravity scales.

In the case when $L \gg L_{eg}$, the bending energy becomes subdominant compared to the gravitational energy, and the film tends to undergo folding with significant out-of-plane deformation when the film is lifted. Indeed, $L_{eg}$ is known to correspond to the typical wavelength of the elastic film under the effect of bottom liquids [18]. A similar argument applies to the present system. On the other hand, when $L \ll L_{eg}$, bending rigidity suppresses large out-of-plane deformation, and the film tends to remain flat and recoil back.

Similarly, when $L \gg L_{ec}$, capillary forces are sufficiently strong, and the film undergoes strong capillary-induced bending deformation as reported for elastocapillary loop structures [16]. When $L \ll L_{ec}$, capillary forces are insufficient to bend the film, and encapsulation of water does not occur

When $L \simeq L_{ec}$ and $L \simeq L_{eg}$, the capillary length $L_{cg} = (\gamma_l/\rho g)^{1/2}$ also becomes comparable to $L$. Therefore, the crossover regime between these characteristic length scales provides a natural condition for liquid encapsulation. This suggests that encapsulation emerges in the crossover regime where bending, capillary, and gravitational effects compete. We also note the relation $L_{eg} = \sqrt{L_{ec} L_{cg}}$, showing that only two independent characteristic scales exist in the present system.

View Article Online
DOI: 10.1039/D6SM00232C



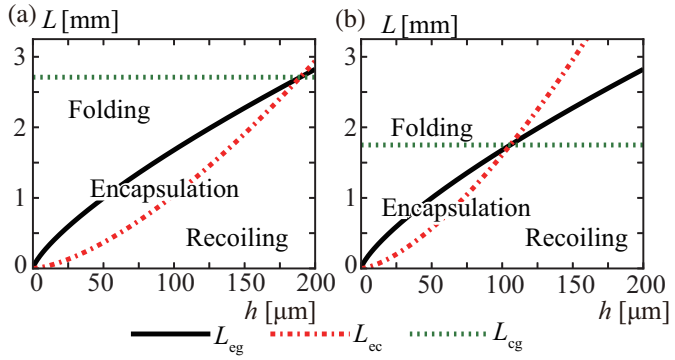


Fig. 4 The characteristic length of the system, elastogravity, $L_{eg}$ (black solid line), elastocapillary, $L_{ec}$ (red dash-dotted line), and capillary length $L_{cg}$ (green dotted line). Each line is drawn based on Eq. (1) with (a) water ($\gamma_w$=72 mN m$^{-1}$) and (b) Triton X solution ($\gamma_T$=30 mN m$^{-1}$)

We note that $B = Eh^3/\{12(1-\nu^2)\}$, where $B$ is proportional to $h^3$. Thus, $L_{eg} \sim h^{3/4}$ and $L_{ec} \sim h^{3/2}$. Using the parameters listed in Table 1, these characteristic lengths are plotted in Fig. 4(a) and (b). As a function of the film thickness $h$, $L_{eg}$ increases as $h^{3/4}$ while $L_{ec}$ increases as $h^{3/2}$. As a result, the two characteristic lengths become comparable over a finite range of $h$, irrespective of the precise numerical prefactors.

This crossover regime corresponds to the parameter range where water encapsulation was observed in the experiments (Fig. 4(a) water and (b) Triton X solution), as seen in the phase diagram shown in Fig. 2(a) and (c). We confirmed the overlapping region shifts toward the lower-left corner when Triton X solution ($\gamma_T$ = 30 mN m$^{-1}$) was used, which is in agreement with Fig. 2(a) and (c).

Here, we note that $L$ should be interpreted as an effective lateral deformation scale of the triangular film, rather than the geometric side length $w$ itself. The deformation is localized along curved ridges as illustrated in Fig. 3, and each energy term depends on the film geometry. As a result, the relevant length scale governing bending, capillary, and gravitational effects depends not only on $w$ but also on the detailed deformation geometry and boundary conditions. Therefore, the plot in Fig. 4 captures the ordering and relative location of the experimentally observed morphology regimes, although the comparison should be understood as semi-quantitative because geometry-dependent numerical prefactors are neglected in the present model.

## 5 Summary and conclusion

In this study, we investigated the lifting and encapsulation of water by an elastic triangular film attached to a vertically moving wire. By systematically varying the film side length, thickness and the surface tension, we identified a limited parameter regime in which the liquid became encapsulated by the film (encapsulation). Outside the encapsulation regime, two other morphologies were observed: folding, in which the film deformed symmetrically while gradually draining the liquid, and recoiling, in which the film returned to a nearly flat configuration after capillary detachment.

Based on simplified geometric assumptions, we confirmed that the film's encapsulation morphology appears in the crossover regime where the elastogravity, elastocapillary, and capillary length scales become comparable. Despite the simplified estimation of these energies, the obtained phase diagram showed semi-quantitative agreement with the experiment.

In this study, we kept the film's lifting speed constant at 1 mm s$^{-1}$. Preliminary experiments suggested that dynamical effects become important when the depth of the liquid reservoir is as small as 1 mm and the liquid viscosity is 1 Pa s so that the effective capillary number for the experiment is of the order of 1. Under such conditions, the dynamic effect should be interesting to consider. We leave this regime for future study.

We note that our system is quasi-static in the sense that the observed morphology is essentially independent of lifting speed. This suggests that the system evolves toward a minimum-energy configuration. However, unlike the capillary origami case[16], the lifting process using a rod attached to the center of the triangular film constrains the deformation pathway. Accordingly, a precise understanding of the phase diagram will require not only length-scale and energy-landscape arguments but also consideration of force balance and dynamical effects, even though most of the observed morphology selection is governed by quasi-static energetics. A full elastodynamic treatment would require appropriate handling of film-edge effects and contact-line dynamics. Such an analysis remains an important direction for future study.

Our results show that simple elastic films can be used to manipulate liquids by appropriately choosing the thickness and side length. For potential application, it would be interesting to consider the effect of handling non-Newtonian liquids with a film for future study. Such approaches may enable the transport and manipulation of liquids and soft materials using simple elastic films.

## Author contributions

Y.T. and Y.S. conceived the experimental design and supervised this study. All experiments were conducted and analyzed by K.S., K.H., Y.T. and Y.S.

## Conflicts of interest

There are no conflicts to declare.

## Data availability

The authors confirm that the data supporting the findings of this study are available within the article.

## Acknowledgements

This work is partially supported by the Grant-in-Aid for Japan Society for Promotion of Science, KAKENHI (Grants No. 16H06478, No. 21H01004, No. 21H01006, No. 26K07037, and No. 26H00387). This work was also supported by JSPS and PAN under the Japan-Poland Research Cooperative Program "Spatio-temporal patterns of elements driven by self-generated, geometrically constrained flows", the JSPS Core-to-Core Program "Advanced core-to-core network for the physics of self-organizing active matter" (JPJSCCA20230002)

View Article Online
DOI: 10.1039/D6SM00232C



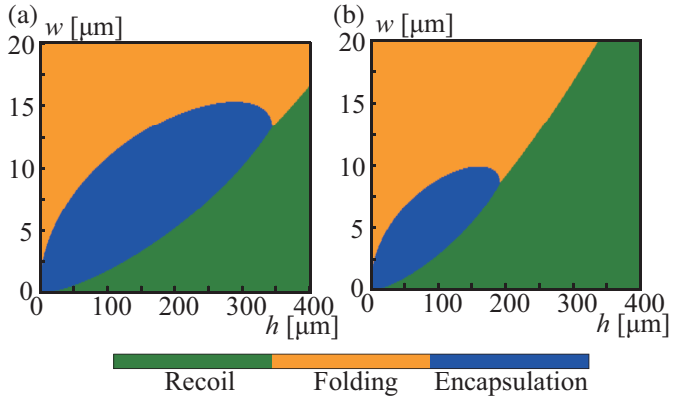


Fig. 5 Energy-minimum phase diagrams calculated from the simplified energy estimates for (a) water ($\gamma_w$=72 mN m$^{-1}$) and (b) Triton X solution ($\gamma_T$=30 mN m$^{-1}$).

## Appendix: Simplified estimation of coefficients in the energy argument

For the simplified energy estimates introduced in the main text, the geometric prefactors can be estimated from the triangular film geometry.

For the recoiling and folding states, the triangular configuration gives $\zeta = \sqrt{3}/4$ and $\xi = \sqrt{3}/2$. For the encapsulated state, assuming a tetrahedron-like liquid volume with ridge structures [Fig. 3(b): Mode II], we estimate the enclosed volume and lifted height as

$$V = \frac{\sqrt{2}}{96} w^3, \qquad \Delta z = \frac{\sqrt{6}}{8} w,$$

which yields $\alpha = \sqrt{3}/384$ for the gravitational energy term. For the bending contribution, using the characteristic area and curvature

$$A = \frac{\sqrt{3}}{4} w^2, \qquad \kappa = \frac{\sqrt{3}}{w},$$

we obtain $\varepsilon = 3\sqrt{3}/4$.

Using these numerical prefactors, we constructed the energy-minimum phase diagrams shown in Fig. 5 for (a) water and (b) Triton X solution.

## Notes and references

1 E. W. Washburn, *Physical Review*, 1921, **17**, 273–283.
2 C. W. Extrand and S. I. Moon, *Langmuir*, 2012, **28**, 15629–15633.
3 M. K. Chaudhury, G. M. Whitesides and G. M. Whitsides, *Science*, 1992, **256**, 1539–1541.
4 Y. Sumino, N. Magome, T. Hamada and K. Yoshikawa, *Phys. Rev. Lett.*, 2005, **94**, 068301.
5 R. W. Style, A. Jagota, C.-Y. Hui and E. R. Dufresne, *Annu. Rev. Condens. Matter Phys.*, 2017, **8**, 99–118.
6 L. Kovanko and S. Tawfick, *Langmuir*, 2019, **35**, 13421–13426.
7 T. Tanaka, M. M. Mitsuaki Morigami and N. A. Nobufumi Atoda, *Jpn. J. Appl. Phys.*, 1993, **32**, 6059.
8 B. Bhushan, *Philos. Trans. R. Soc. A*, 2019, **377**, 20190119.
9 M. Shimamura, *Plant Cell Physiol.*, 2016, **57**, 230–256.
10 J. Ju, H. Bai, Y. Zheng, T. Zhao, R. Fang and L. Jiang, *Nat. Commun.*, 2012, **3**, 1247.
11 D. L. Hu and J. W. M. Bush, *Nature*, 2005, **437**, 733–736.
12 D. L. Hu, B. Chan and J. W. M. Bush, *Nature*, 2003, **424**, 663–666.
13 X. Gao and L. Jiang, *Nature*, 2004, **432**, 36–36.
14 M. Yoshii, H. Yamamoto, Y. Sumino and S. Nakata, *Langmuir*, 2016, **32**, 3901–3906.
15 H. Zhu, B. Xu, Y. Wang, X. Pan, Z. Qu and Y. Mei, *Sci. Robot.*, 2021, **6**, eabe7925.
16 C. Py, P. Reverdy, L. Doppler, J. Bico, B. Roman and C. N. Baroud, *Phys. Rev. Lett.*, 2007, **98**, 156103.
17 J. Bico, E. Reyssat and B. Roman, *Annu. Rev. Fluid Mech.*, 2018, **50**, 629–659.
18 P. M. Reis, J. Hure, S. Jung, J. W. Bush and C. Clanet, *Soft Matter*, 2010, **6**, 5705–5708.
19 K. Nakamura, T. Hisanaga, K. Fujimoto, K. Nakajima and H. Wada, *J. R. Soc. Interface*, 2018, **15**, 20170868.
20 M. L. Fitzgerald, S. Tsai, L. M. Bellan, R. Sappington, Y. Xu and D. Li, *Biomed. Microdevices*, 2019, **21**, 1–8.
21 B. Roman and J. Bico, *J. Phys. Condens. Matter*, 2010, **22**, 493101.

View Article Online
DOI: 10.1039/D6SM00232C

The authors confirm that the data supporting the findings of this study are available within the article.